Version of Record: https://www.sciencedirect.com/science/article/pii/S1359645421009927
Manuscript_d0b26eeeb297a1420010781890b59333

Grain Size Dependencies of Intergranular Solute Segregation in Nanocrystalline Materials

Nutth Tuchinda[1], Christopher A. Schuh[1*]

[1]Department of Materials Science and Engineering, Massachusetts Institute of Technology, 77 Massachusetts Avenue, Cambridge, MA, 02139, USA

***Correspondence to: schuh@mit.edu**

Abstract

Grain boundary segregation is of increasing importance for stabilizing nanocrystalline alloys, and while segregation is typically modeled as a scale-independent phenomenon, at the finest nanocrystalline grain sizes there are several sources of grain size dependence. Here we provide quantitative detail on two grain size dependencies not previously elaborated, both of which arise from the spectrality of intergranular segregation sites. The first of these arises because a change in grain size affects which portions of the segregation spectrum are occupied by the solutes, with no change in the shape or nature of the spectrum itself. The second of these arises from the presence of higher-order grain junctions, which have unique segregation behaviors and an increasing relative presence at finer grain sizes. This paper uses molecular statics to quantify these size dependencies in detail for the case of an Al(Mg) binary alloy. Together, these two effects combined have a significant effect on the effective McLean segregation energy of more than 6 kJ/mol (from approximately -18.5 kJ/mol at 5 nm to -12.5 kJ/mol at more than 40 nm), with the majority of grain size dependence arises from the spectrality of segregation sites.

Keywords: Grain Boundary, Triple junction, Quadruple Node, Segregation, Nanocrystalline, Thermodynamics, Atomistic Simulation

---

1. Introduction

The high volume fraction of grain boundaries in nanocrystalline materials can lead to instability and rapid grain growth. For this reason, grain boundary solute segregation has been widely explored and used by the community to hinder grain growth both kinetically [1–6] and thermodynamically [7–14]. As a result, researchers are increasingly trying to design alloys with the specific intention of inducing grain boundary segregation. For these purposes, simple design criteria [13,15,16] that use an "average" grain boundary segregation energy are often used as screening tools. This is in line with the classical isotherm approach to grain boundary segregation as proposed by McLean [17], which classifies atomic sites into two types, grain boundary and crystalline sites, with the assumption of constant segregation energy at all viable grain boundary sites:

$$\frac{\bar{X}^{IG}}{1-\bar{X}^{IG}} = \frac{X^C}{1-X^C} exp\left[-\frac{\Delta E^{seg}}{k_b T}\right] \quad (1)$$

Here $\bar{X}^{IG}$ and X^C are the average solute concentration in the intergranular network and crystalline regions, respectively, and ΔE^{seg} is segregation energy which reflects the energetic difference between bulk crystalline and intergranular solute. Here and below we take the definition that negative values of ΔE^{seg} are associated with a preference for grain boundary segregation (although it should be noted that this is opposite of the sign convention taken by McLean in his original work).

The isotherm approach described above, as well as a vast literature of related work [18–20], are based on an "open system" assumption, where an infinite reservoir of crystalline sites are available to equilibrate with the grain boundary. This assumption results in the equivalence $X^c = X^{tot}$, the total concentration of solute in the system. With the early experimental observations of size-dependent segregation [21,22], Ishida [20] pointed out that for fine grain sizes this approximation fails, and corrected it with a simple solute balance equation:

$$X^{tot} = (1-f^{IG})X^C + f^{IG}\bar{X}^{IG} \quad (2)$$

where f^{IG} is the intergranular site fraction. This is the first source of apparent size dependence of segregation behavior, because the intergranular and crystalline site fractions now vary with grain size, which in turn shifts the balance of solute partitioning via Eq. (2). This geometrical grain size dependence is illustrated in Fig. 1a at two different grain sizes; at constant composition a reduction of grain size leads to lower solute population of the grain boundary sites. This size dependency is now widely recognized and corrected for in small computational systems or at fine grain sizes [23–29].

There are, however, other sources of grain size dependence on intergranular segregation that are not yet widely recognized or accounted for, with special relevance in nanocrystalline metals. These result from the physical nature of segregation as a spectral problem; the excess energy and segregation energy are not single-valued, but in fact very widely distributed over a multitude of different atomic sites. In bulk nanocrystalline materials this is especially important due to the vast grain boundary space presented in polycrystals [26,30], given the high volume fraction of grain boundary atoms. For such cases the local concentration at a given site-type *i* can be calculated using a specific site segregation energy ΔE_i^{seg} instead of a single value ΔE^{seg} [31]:

$$\frac{X_i^{IG}}{1-X_i^{IG}} = \frac{X^C}{1-X^C} exp\left[-\frac{\Delta E_i^{seg}}{k_b T}\right] \quad (3)$$

where X_i^{IG} describes the solute concentration at site type *i* with segregation energy ΔE_i^{seg}.

When this expression is combined with information on the complete distribution of sites available in a polycrystal, it can be used to compute the average solute excess and effective

segregation energy of the ensemble. In polycrystals, for example, it has been proposed that the distribution of segregation energies can be approximated as a skew-normal distribution [25,32]:

$$F_i = \frac{1}{\sqrt{2\pi}\sigma}\exp\left[-\frac{\left(\Delta E_i^{seg}-\mu\right)^2}{2\sigma^2}\right] erfc\left[\frac{\alpha\left(\Delta E_i^{seg}-\mu\right)}{\sqrt{2}\sigma}\right] \quad (4)$$

where F_i is the intergranular site probability density function, which is described by shape (α), location (μ), and scale (σ) parameters, alloy-specific quantities that have been tabulated for a number of alloys in Ref. [26].

When the McLean-type assumption of a single segregation energy is replaced by a distribution of intergranular sites in this manner, there is an additional Ishida-like size effect with a more complex solute conservation law than Eq. (2), to account for a multitude of intergranular site types. This spectral effect is schematized in Fig. 1b, where smaller grains lead to a significantly different distribution of solute in grain boundary regions, and less grain boundary segregation in total. A lower average grain boundary segregation energy is therefore seen at fine grains. Because full-spectra studies of grain boundary segregation remain scarce, we are not aware of any quantitative elaboration of this spectral effect as yet.

Spectrality can also lead to a physical size effect at the very smallest nanoscale grain sizes. At scales below about 20-30 nm, triple junction lines and quadruple nodes become increasingly relevant in terms of their atomic participation [33,34]. These changes in the structure of the grain boundary network itself can manifest in the segregation energy distribution of Eq. (4) if, e.g., triple junctions present unique sites for segregation as compared with the boundaries themselves. This hypothesis is supported by the literature in the specific case of solute segregation that both experimentally measured local concentrations [35–37] and computational results [38,39] suggest unique triple junction behavior. Fig. 1c schematizes this scenario, where the full intergranular spectrum changes at fine grain sizes due to the participation of higher-order junctions in the problem.

Our goal in this paper is to explicitly demonstrate and quantify the grain size dependence of segregation behavior in the dilute limit caused by these latter two issues, namely, Ishida-like grain size-dependencies caused by spectrality (Fig. 1b) and grain size-dependencies due to the scaling of higher-order junction fractions in intergranular networks (Fig. 1c). Using atomistic simulations on a specific model system (Al-Mg) we demonstrate that the scaling behavior of overall intergranular excess and effective segregation energy at the finest grain sizes indeed are significantly dependent upon both the fraction of intergranular sites as well as the relative prominence of higher-order junctions. The framework established here should be applicable to binary alloys in general.

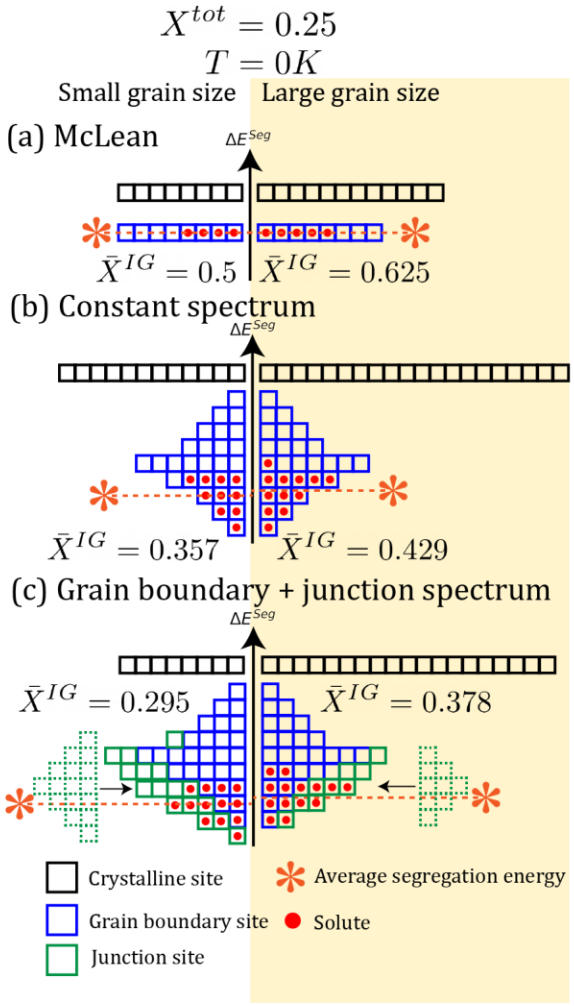

Fig. 1. Schematic of intergranular segregation at T = 0 K with a fixed solute fraction X^{tot} = 0.25 and (a) classical McLean model assuming a single average segregation energy, (b) a constant segregation spectrum and (c) a grain-size dependent spectrum due to the presence of grain junctions. Changes in the grain size in each case lead to reapportioning of the solutes amongst the available site-types, as demonstrated by solute occupation of the lowest energy sites.

2. Intergranular Segregation: Definitions and Framework

Segregation energy is defined as the energy of the fully relaxed system with the solute in an intergranular site i (E_i^{seg}) minus the energy of the relaxed system with the solute in a bulk crystalline site (E^{bulk}):

$$\Delta E_i^{seg} = E_i^{seg} - E^{bulk} \tag{5}$$

In this work, for simplicity the energy of segregation is calculated using molecular statics, which implies an assumption of negligible system volume change, and neglects excess (nonconfigurational) entropy of segregation; all energies are internal energies. As we develop the methodology in this section, we focus on Al with a dilute addition of Mg as the solute, using the

embedded atom method (EAM) potential for the binary Al(Mg) system [40]. This interatomic potential has been used for studies of intergranular segregation by Refs. [25,27,30,41–43] and the dilute-limit segregation spectrum has been explored in detail in Ref. [25] for comparison. For this system the reference alloying energy E^{bulk}, the substitutional energy of placing a solute on the solvent crystalline lattice, is E^{bulk} = 2.0040±0.0025 eV.

For the conservation of solute, global solute concentration, X^{tot}, relates to the mean intergranular concentration, $\bar{X}^{IG}$, intergranular atomic site fraction, f^{IG} , and F_i^s, the fraction of site type 'i' in the defect type 's', with s denoting grain boundaries (GB), triple junctions (TJ), quadruple nodes (QN) or the entire intergranular network (IG) inclusive of all GBs, TJs and QNs, i.e. $f^{IG} = f^{GB} + f^{TJ} + f^{QN}$. This gives an expansion of Eq. (2) as:

$$X^{tot} = (1 - f^{IG})X^C + f^{IG}\bar{X}^{IG} = \left(1 - \sum_s f^s\right)X^C + \sum_s f^s\,\bar{X}^{IG} \tag{6}$$

where

$$\bar{X}^{IG} = \sum_i F_i^{IG} X_i \tag{7}$$

and

$$\sum_i F_i^{IG} = \sum_i \sum_s F_i^s = \sum_i F_i^{GB} + \sum_i F_i^{TJ} + \sum_i F_i^{QN} = 1 \tag{8}$$

The mean concentration at defect type 's' can then be calculated by averaging all sites of that type:

$$\bar{X}^s = \sum_i F_i^{s,norm} X_i^s \tag{9}$$

where $F_i^{s,norm}$ is the normalized site fraction of site type 'i' in the defect type 's' that follows:

$$\sum_i F_i^{s,norm} = 1 \tag{10}$$

For the form presented in Eq. (6-10), F_i^s, represents the partial site fraction in the whole intergranular network while the normalized form, $F_i^{s,norm}$, indicates the fraction of site type 'i' within its own defect type. In a similar manner, an "effective" segregation energy ($\Delta\bar{E}_{Eff}^s$) can be calculated by solving the equation:

$$\frac{\bar{X}^s}{1 - \bar{X}^s} = \frac{X^C}{1 - X^C} exp\left[-\frac{\Delta\bar{E}_{eff}^s}{k_b T}\right] \tag{11}$$

and is equivalent to a single-value segregation energy in the McLean segregation isotherm that would achieve the same concentration as the spectral model. The current thermodynamic framework is essentially an extension of the White and Stein model [31], grouping sites by their defect type, 's', and cognizant of solute balance in the manner of Eq. (2) by Ishida [20].

The above framework can also be cast in a continuous form by replacing summations with integrals:

$$\bar{X}^{IG} = \sum_s \int d\Delta E_i^{seg} \, F_i^s\left(\Delta E_i^{seg}\right) X_i\left(\Delta E_i^{seg}\right) \tag{12}$$

$$\sum_s \int_{-\infty}^{\infty} d\Delta E_i^{seg} F_i^s(\Delta E_i^{seg}) = 1 \tag{13}$$

$$\bar{X}^s = \int_{-\infty}^{\infty} d\Delta E_i^{seg} F_i^{s,norm}(\Delta E_i^{seg}) X_i^s \tag{14}$$

$$F_i^s\left(\Delta E_i^{seg}\right) = \frac{f^s}{f^{IG}} F_i^{s,norm}\left(\Delta E_i^{seg}\right) \tag{15}$$

where the $F_i^s\left(\Delta E_i^{seg}\right)$ denote site probability density functions instead of site fractions in the discrete spectrum model.

The continuum framework of Eqs. (12-15), combined with the skew-normal approximation approach of Eq. (4), can be applied to interpolate and extrapolate intergranular segregation inclusive of the GB, TJ, and QN subspectra, which can each have their own distribution functions. This will help elucidate the grain size dependency of segregation due to the presence of TJs and QNs. It is important to stress that the thermodynamic framework used here is a dilute-limit model; it does not contain any treatment for solute-solute interactions. In this work, the solutions from the discrete spectra, Eqs. (3, 6-11), are labeled as "discrete" and the continuous framework utilizing skew-normal distribution and Eqs. (3-4, 6, 11-15) are called "continuous". Monte Carlo ("MC") can alternatively be used to solve for the segregation state, using the segregation energies from molecular statics to determine solvent-solute site-swapping probabilities. All of these methods produce the same results, as described in detail in Ref. [25], and can therefore be used interchangeably.

3. Grain Boundary Network Geometry

Since we are interested in effects of grain size and the relative prominence of higher-order grain junctions upon intergranular segregation, we require a system geometry designed to hold all other variables essentially constant. We therefore build a single polycrystalline structure and rescale it to maintain the same specific defect crystallographies, while changing the grain size. Using the potential for Al from Ref. [40], a reference polycrystalline sample with 14 grains is randomly generated using Atomsk [44]. The fractional positions of grain centers in the simulation cell are then used to generate polycrystals with different grain sizes while maintaining self-similarity of the microstructure, as shown in Fig. 2, keeping constant the orientations of the grains. While it is difficult to cover all possible grain boundary crystallographies (let alone triple junction crystallographies), this structure was selected because it is large enough to provide a

reasonable degree of coverage over misorientation space, as shown for the 82 grain boundaries in the structure in Fig. 3 plotted by the MTEX software package [45] after annealing.

The grain boundary planes in these simulations are those that form under equilibration in this configuration. Specifically, after generation, each polycrystal is annealed at 0.2 T_{melt} for 50 ps then cooled to 0 K at 2 K/ps with a timestep of 1 fs, conditions chosen to maintain grain boundary network self-similarity while still relaxing the boundaries. Both annealing and cooling are done using the Nose-Hoover algorithm at zero pressure with the Large-scale Atomic/Molecular Massively Parallel Simulator (LAMMPS) software package [46–49]. Thus, although we do not explicitly sample the grain boundary plane in a statistical fashion, we do insure that the planes sampled are energetically appropriate for the misorientations constructed.

For grain segmentation, we use the polyhedral template matching (PTM) method [50] implemented in the OVITO software package [51] to identify local lattice orientation. Using an angle tolerance of 1^o with a minimum grain size of 200 atoms, each grain is individually numbered and each atom is assigned to one grain. The grain segmentation algorithm follows Ref. [52] but with lattice orientations calculated from PTM. After grain segmentation, we employ nearest neighbor searches around non-FCC atoms, which are identified by adaptive common neighbor analysis [53,54] with a cutoff radius of 0.6 nm, and if there are two, three, or four distinct grain numbers in this neighborhood, the atom is then assigned as a grain boundary (GB), triple junction (TJ), or quadruple node (QN) atom, respectively. This leads to the average quadruple node population of about 35 atoms. Although the atomic volume of GB, TJ and QN atoms differ from FCC lattice, for comparison, the first three nearest neighbor shells of FCC-Al consist of 43 atoms.

By assuming a constant grain boundary thickness, simple geometrical analysis can be used to connect grain size to volume fractions of the various atomic site types. For example, Wang et al. assumed an ideal tetrakaidecahedron grain geometry with an edge length of $l + \Delta$ enclosing one with edge length l [34], to derive the volume fractions f^s for grain boundaries (s = GB), triple junctions (s = TJ) and quadruple nodes (s = QN) as:

$$f^{GB} = 3x^3 - 6x^2 + 3x \tag{16}$$

$$f^{TJ} = -3x^3 + 3x^2 \tag{17}$$

$$f^{QN} = x^3 \tag{18}$$

where $x = \Delta/(l + \Delta)$ is referred to as a relative grain boundary thickness. While the scaling laws encapsulated in Eqs. (16-18) are expected to be independent of grain shape, the coefficients are grain shape dependent. The meaning of 'grain size' may change with geometry as well, i.e., from edge length of a tetrakaidekahedron to diameter of a sphere, etc. To generalize this geometrical approach, we write similar polynomials, but explicitly define the grain size, *d*, as the

average spherical equivalent grain diameter and permit the coefficients to be tuned to account for different grain shapes:

$$f^s = A_3^s \left(\frac{a}{d}\right)^3 + A_2^s \left(\frac{a}{d}\right)^2 + A_1^s \left(\frac{a}{d}\right) \tag{19}$$

$$d = 2\frac{L}{(N\frac{4}{3}\pi)^{1/3}} \tag{20}$$

Here a is an intergranular dimension, similar to Δ, L is the computational system size, with N grains. The grain sizes with the corresponding system size are listed in Table 1 for the ease of comparison. The A_i^s are polynomial coefficients which are characteristic of a specific grain structure.

Our simulated polycrystals can be used to calibrate the unknown coefficients and a in Eq. (19), because each atom is identified uniquely with a single atomic site type, s. Fig. 4 shows the computed atomic fractions of all the site types, for all 13 self-similar grain structures. The best-fitted form of Eq. (19) is also shown for comparison, the results of which are listed in Table 2. The polynomials are fitted subject to a convergence constraint of $f^{IG} = f^{GB} + f^{TJ} + f^{QN} = 1$ at $d = a$, which has a specific value of 1.810 nm for the current structures. These values will be useful in what follows to scale grain boundary segregation distributions proportionally to the atomic fractions of each species, and therefore to extrapolate segregation behavior to other grain sizes not considered.

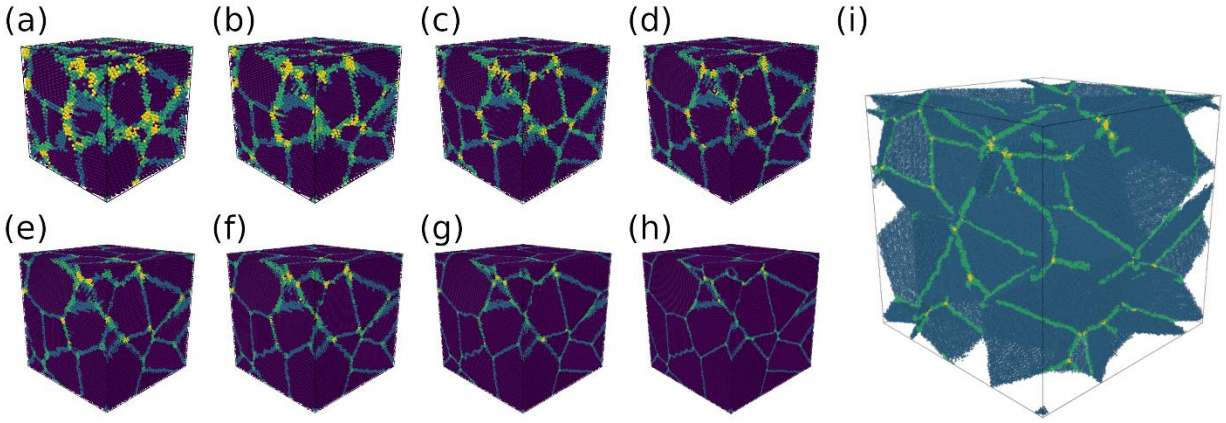

Fig. 2. The series of geometrically- and crystallographically-self-similar structures used in this work, with system edge lengths of 10.0 (a), 12.5 (b), 15.0 (c), 17.5 (d), 20.0 (e), 22.5 (f), 30.0 (g), and 40.0 nm (h). Panel (i) shows the grain boundary network of the 40.0 nm system with crystalline atoms made transparent. In all panels, the atoms are colored by their environment type, as crystalline (purple), grain boundary (teal), triple junction (green) and quadruple node (yellow).

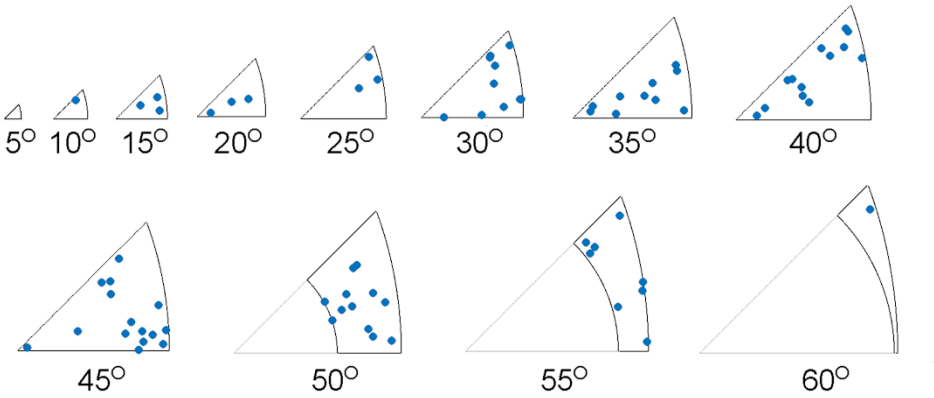

Fig. 3. Misorientation distribution of the 82 grain boundaries in the simulated polycrystals using fundamental zone binning of the cubic symmetry group [55].

Table 1 System and spherical equivalent grain sizes (*d*)

System Size (nm)	Spherical Equivalent Grain size (nm)
10.0	5.15
12.5	6.43
15.0	7.72
17.5	9.01
20.0	10.30
22.5	11.58
30.0	15.44
40.0	20.59

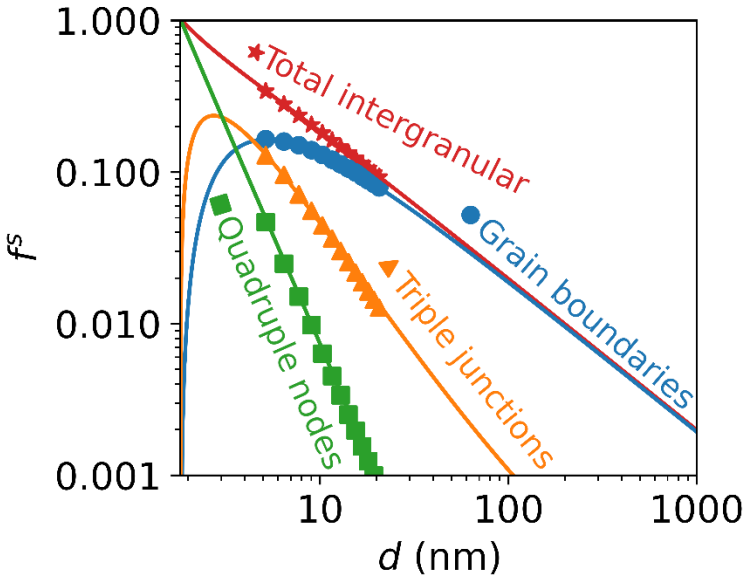

Fig. 4. Defect fractions of the simulated polycrystals, fitted by the modified polynomials of grain boundary atomic fraction (f^{GB}), triple junction atomic fraction (f^{TJ}) and quadruple node atomic fraction(f^{QN}).

Table 2 Fitted grain geometry parameters for f^s, for use with Eqs. (20)

s	a (nm)	A_3	A_2	A_1
GB		1.00	-2.08	1.07
TJ	1.81	-1.54	1.51	0.0333
QN		0.951	0.0817	-0.00510

4. Assessing the Segregation Spectra

The segregation energy spectra are calculated following the method of Ref. [25], which proposes a direct one-by-one solute substitution on each defect site in the structure followed by conjugate gradient minimization for structural relaxation. The resulting system energy gives the value of the dilute E_i^{seg} for site 'i', for use with Eq. (3). As an example, the total intergranular segregation spectrum is shown in Fig. 5 for the case of d = 5.15 nm. The result here closely matches the calculated spectra by Wagih and Schuh for the same alloy system [25,26]. However, with the present method, we are able to separate out individual subspectra for the GBs, TJs, and QNs. These normalized subspectra are also highlighted in Fig. 5a, and clearly are distinct from one another and from the total spectrum; the GBs, TJs, and QNs contribute unique sets of segregation sites to the structure. The spectra can also be represented normalized to their respective defect fractions to illustrate the relative importance of each defect type's contribution to the total spectrum, as shown in Fig. 5b, although this mode of presentation does not reflect the distinct energetic states of the defect types as clearly as does the presentation in Fig. 5a.

Although the GBs, TJs, and QNs have distinctly different segregation site spectra, as seen in Fig. 5a, these subspectra are themselves effectively grain size independent. This is explored in more detail in Fig. 6. In Fig. 6a all of the distributions are shown, broken out by defect type. The results for all investigated grain sizes lie atop one another to within error: the intrinsic segregation distributions are characteristic of defect type specifically. The same data plotted as a function of grain sizes are represented by the box-whisker plots in Supplementary Fig. 2. These segregation energy spectra are fitted with a skew-normal distribution (cf. Eq. (4)) and the results are listed in Table 3 and Supplementary Table 1. As expected based on the observations in Figs. 5 and 6, the fitted distribution parameters speak to greater segregation tendency (lower μ most obviously) for higher-order defects.

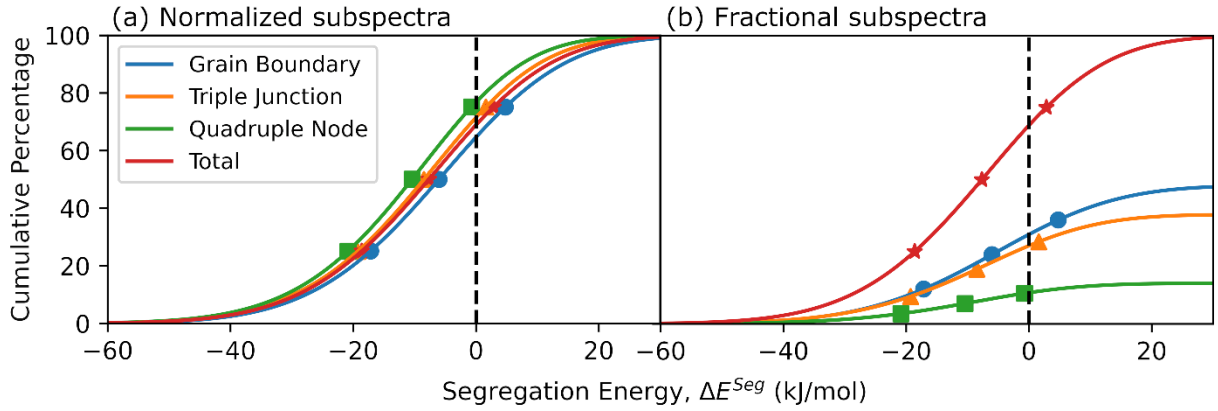

Fig. 5. Normalized segregation subspectra (a) and fractional subspectra (b) of the system with the grain size of d = 5.15 nm. Fractional subspectra of grain boundary (●, blue), triple junction (▲, yellow) and quadruple node (■, green) sites are scaled according to the defect fraction in the intergranular network, which add up to the total spectrum labeled in red (*).

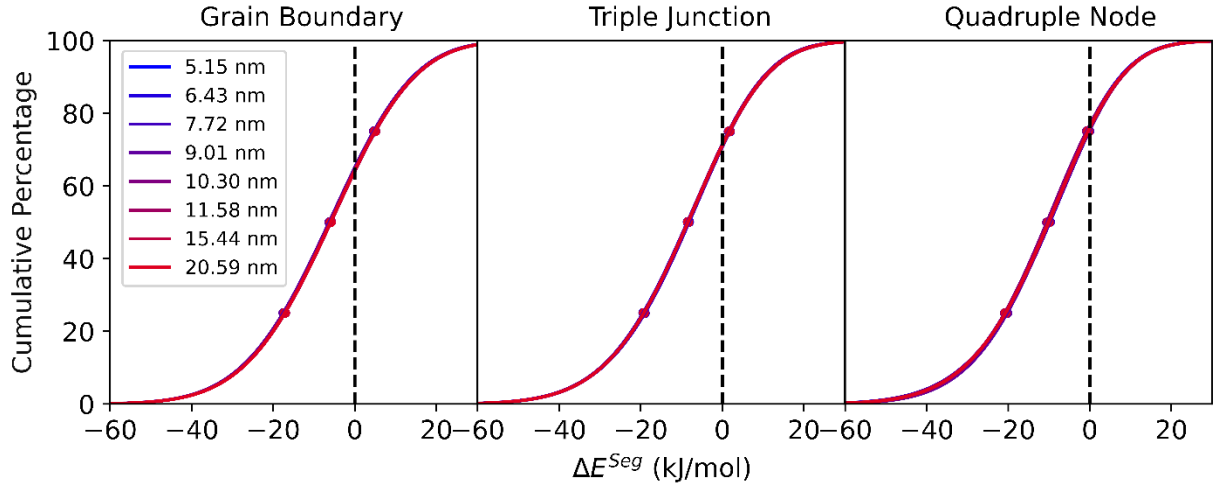

Fig. 6. The cumulative distribution functions of grain boundary, triple junction and quadruple node spectra, which are found to be effectively independent of grain size.

Table 3 Fitted skew-normal distribution parameter of the system with d = 5.15 nm grain size

Defect Type	α	μ (kJ/mol)	σ (kJ/mol)
GB	-1.06	5.21	20.1
TJ	-1.48	4.51	20.9
QN	-1.55	2.38	20.4
Total IG	-1.19	4.13	20.2

5. Ishida-type Grain size-dependence caused by Intergranular Site Spectrality

As noted in the Introduction, Ishida [20] first noted the geometrical grain size effect related to changing site fractions as in Eq. (2) and Fig. 1a. When there are more site types present, such effects not only persist, but can become even more pronounced, as schematized in Fig. 1b. In this section, we explore this issue quantitatively. In order to separate this issue from the effects of higher-order junctions, we can explicitly take only the GB subspectrum from Fig. 6, neglecting the higher-order junctions, and perform an analysis of grain size dependence on it directly.

A full calculation of this spectrality grain size dependence at finite temperature is shown in Fig. 7 and 8, obtained by computing the site occupation without the contributions of the higher-order junction sites. We maintain the intergranular site fraction constant by rescaling according to the fitted polynomials in Fig. 4, so that the correct number of intergranular sites are always available, but they are all of the GB type at all grain sizes. Fig. 7a shows the site occupancy at X^{tot} = 0.05 and T = 700 K, with a large spike representing the crystalline sites at $\Delta E^{seg} = 0$. As grain size increases, we see the shift in the availability of intergranular and bulk sites, with more bulk sites at larger grain sizes. This results in more intergranular site occupancy at larger grain sizes observed by the shifts of the occupancy peak in Fig. 7a. It shall be noted here that Fig. 7 is plotted with a semi-log scale and hence the site density at the positive and negative tail of the distributions may appear as being omitted. They indeed exist in the spectra as shown in Fig. 5 and 6.

In contrast to this result, the simpler two-state McLean site occupancy with $\Delta E^{seg} = -15$ kJ/mol is shown in Fig. 7b. As demonstrated by Ref. [25], the choice of this average segregation energy is arbitrary and depends on the temperature and concentration used for fitting. We choose -15 kJ/mol as an example case since this value can reproduce behavior at small grain sizes close to the spectral model (cf. Fig. 8a). More demonstrations of the choice of this average segregation energy can be found in the Supplementary Fig. 2. This case does not exhibit spectrality; while a single GB site type does lead to the Ishida grain size dependence, it misses the nuance of the redistribution of solute over the GB spectrum, and thus misses an additional grain size dependence. This is explored in Fig. 8a-c, where each of the compositions is presented explicitly as a function of grain size. (We note that all methods of analysis (continuous, discrete and MC

as described in the procedural section) produce the same result here, as demonstrated in Supplementary Fig. 2 and 3.)

All these panels show an excess grain size dependence from spectrality, but Fig. 8c most concisely summarizes the net effect that the segregation excess, $\bar{X}^{IG}/X^{C}$, has a significantly steeper slope owing to the use of the full site spectrum as compared to the classical McLean isotherm. This corresponds in turn to a grain size-dependence of the effective segregation energy, $\Delta\bar{E}_{eff}^{seg}$, as shown in Fig. 8d.

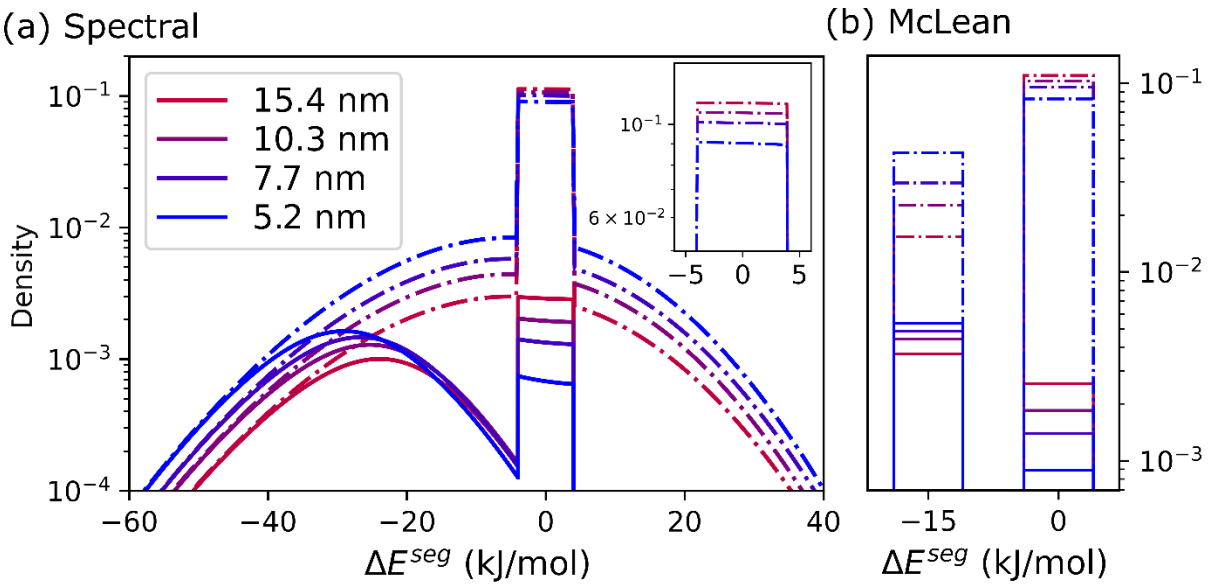

Fig. 7. Solute site occupancy at X^{tot} = 0.05 and T = 700 K of selected grain sizes using (a) calculated GB subspectra and (b) a constant McLean segregation energy of -15 kJ/mol. The dashed-dot lines represent site density (areas under the curves are unity) with the solute occupancy with the solid lines.(i.e. all solid lines can be integrated to X^{tot} = 0.05).

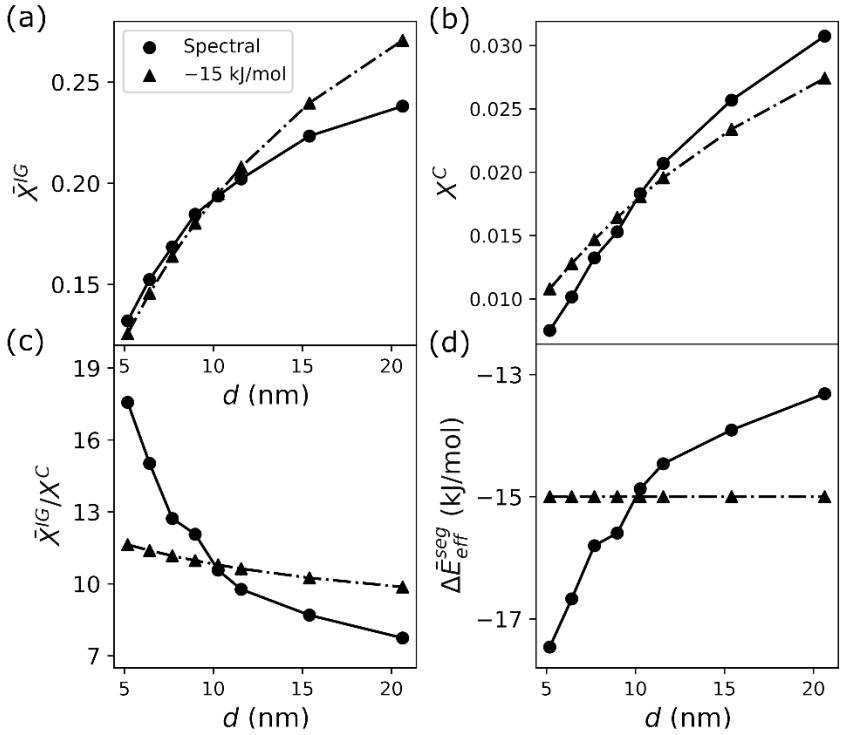

Fig. 8. Grain size-dependence of (a) Intergranular solute concentration, $\bar{X}^{IG}$, (b) crystalline concentration, X^C, (c) solute excess, $\bar{X}^{IG}/X^C$, and (d) effective segregation energy, $\Delta\bar{E}_{eff}^{seg}$, at X^{tot} = 0.05 and T = 700 K. Solid lines (·●) represent the spectral framework while the dashed-dot lines (▲) with a single segregation energy of -15 kJ/mol (McLean isotherm) is shown for comparison with the dilute spectral model.

6. Grain Size Effects Due To Triple Junctions and Quadruple Nodes

The spectra shown in Figs. 5 and 6 reveal that in polycrystals, TJs and QNs provide unique sites for intergranular segregation, and although all intergranular regions are generally favorable for segregation, the higher-order junctions are the most favorable in the present Al(Mg) alloy. To show the extent to which those TJ and QN sites affect local solute concentration differences, we proceed to evaluate the average concentration and effective segregation energy in equilibrated systems. It should be noted that the dilute limit approximation is valid up to approximately 10% solute in the intergranular network in this Al(Mg) system [27], although here for the sake of better comparison we go beyond this level to more than 40% solute; this also permits comparison with Ref. [25] which has examined this particular spectrum in detail.

The results are shown in Fig. 9, and looking first at Fig. 9a-b we see that with higher-order junction concentrations present, we achieve intergranular concentrations higher than typical GB concentrations alone. By the same token, the effective segregation energies of those higher-order defects are more favorable for segregation than the GBs, as seen in Fig. 9c. These results can also be deconstructed to identify local values for the individual GBs, TJs, and QNs (of which

there are respectively 82, 158, and 92 in the present case). We achieve this by grouping intergranular atoms according to their nearest neighbor grains. The effective segregation energy at each individual GB, TJ, and QN are plotted in Fig. 10 to illustrate the degree of anisotropy that might be seen if individual defects were to be sampled in polycrystals. It is clearly seen that the spectrum of higher-order junction characteristics gives rise to a greater breadth of individual segregation energies than to the GBs alone. Thus, sampling of TJs and QNs via experimental methods requires adequate sampling across the junction space and the results obtained from a small sample size should be carefully interpreted. Lastly, we shall note that the neglected solute interactions for this specific interatomic potential [40] are expected to be positive (less segregation compared to the dilute limit) and can be included with the model described in Ref. [27].

Since the segregation subspectrum of the defect types is independent of grain size (cf. Fig. 6), the primary effect of grain size on the total segregation spectrum due to these features is their changing relative prominence in the intergranular network. To clearly see the grain size dependency, equilibrium intergranular concentration, crystalline concentration, solute excess, and effective segregation energy are plotted in Fig. 11 for all simulated systems (using the discrete framework). We also show the analytical results of the continuous distribution formalism, which extrapolates (Eq. (15)) using the defect subspectra of the system from the smallest grain size in this study.

There is a true grain size dependence in both the segregated solute content (Fig. 11a-b) as well as the effective segregation energy (Fig. 11c) of the intergranular network due to the higher-order junction subspectra. Eq. (15) and (19) allow us to interpolate and extrapolate, resulting in the solid lines in Fig. 11d-f. The dashed lines are calculated with GB subspectrum parameters such as used in the previous section, so they only reflect the cases where grain junction effects are neglected. The primary grain size dependence seen here (the curvature of the trendlines) is therefore due to site spectrality, while the difference between the solid and dashed lines captures the additional increment of grain size dependence caused by the increasing presence of higher-order junctions at small grain sizes. The magnitude of the junction subspectral shifts are less than the average segregation energy itself, and the junctions account for approximately 22% of the net grain size-dependence in this system (Grain junctions give rise to the $\Delta\bar{E}_{eff}^{seg}$ shift of roughly 1.3 kJ/mol compared to the total grain size dependence of approximately 6 kJ/mol in Fig. 11f.). For comparison, the results from the classical McLean isotherm are demonstrated here to show that the spectrality of segregation sites can significantly amplify Ishida's size effect. This stresses the importance of the size effects in the context of intergranular solute segregation.

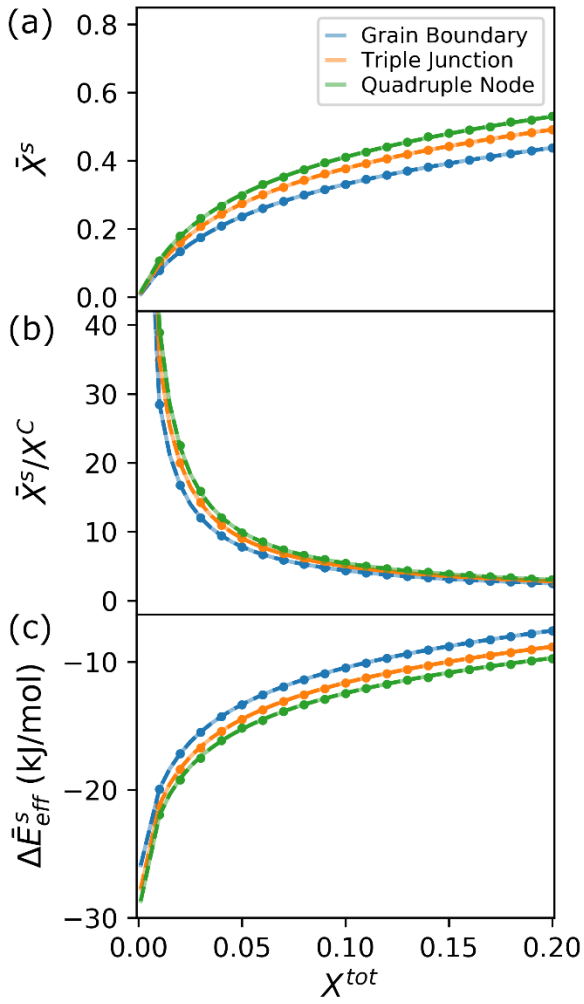

Fig. 9. Grain boundary, triple junction and quadruple node concentration (a), solute excess (b) and effective segregation energy (c) calculated from the discrete (solid lines), continuous (dashed lines) and MC (dots) framework of Al-Mg system with d = 20.59 nm at T = 700 K.

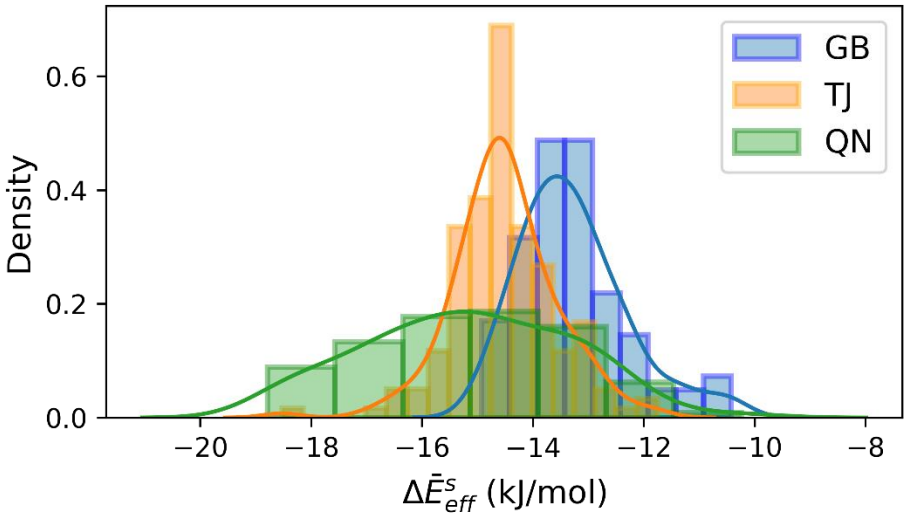

Fig. 10. Distribution of effective segregation energy of grain boundaries , triple junctions , and quadruple nodes of the system with d = 20.59 nm at X^{tot} = 0.05 and T = 700 K.

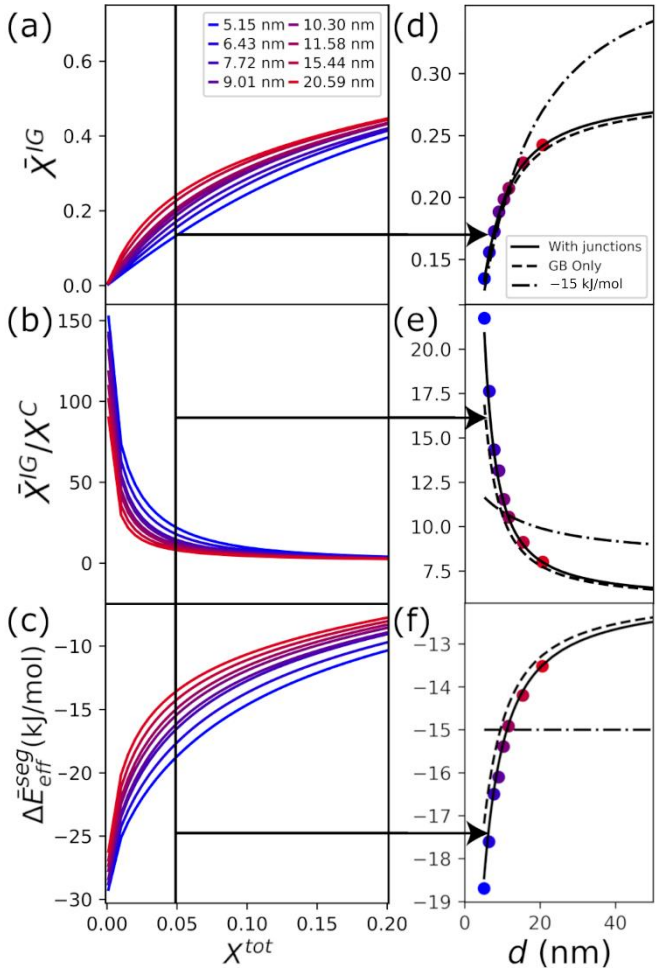

Fig. 11. Grain size dependency of (a) total intergranular concentration, (b) intergranular excess, and (c) effective segregation energy at 700 K calculated from the full discrete spectra. The subspectra from the finest grain size (d = 5.15 nm) polycrystal are combined with the defect fraction polynomials from Eq. (8) and Table 2 to produce extrapolated (d) $\bar{X}^{IG}$, (e) $\bar{X}^{IG}/X^{C}$ and (f) $\Delta\bar{E}_{eff}^{seg}$ on the right (solid lines) which match the full discrete spectra (dot markers). Dashed lines calculated with only the grain boundary subspectrum and dash-dot lines with the McLean segregation energy of -15 kJ/mol are added to demonstrate the extent of junction effects.

7. Conclusion

In summary, we have presented a quantitative assessment of two new sources of grain size dependence caused by site spectrality in the intergranular solute segregation behavior of nanocrystalline materials. Using a defect identifying algorithm on a specific alloy Al(Mg), over a range of polycrystalline grain sizes, we separated effects of site spectrality and higher-order defects on dilute-limit intergranular segregation. The methodology presented here should be generalizable to other systems, and the physics of grain size dependent segregation in the present system are first examples of what could be canonical behaviors:

- The dilute defect (GB, TJ and QN) segregation subspectra of Al(Mg) polycrystals are effectively grain-size independent within the grain size range of 5-20 nm and can be approximated with a skew-normal distribution. When subspectra are combined, the total spectrum exhibits grain size dependency due to defect fraction scaling described by the polynomials from Eq. (19). This allows extrapolation via the dilute-limit framework with Eq. (15).
- In the Al(Mg) binary system [40], junction subspectra are shown to prefer segregation even more strongly than the GB subspectra, leading to increased segregation at the finest grain sizes.
- Even without the effects of higher-order junctions, site spectrality alone causes a significant grain-size dependency well beyond that expected from the classical McLean model, due to increases in the grain boundary coverage with grain size. This results in the grain-size dependence of solute distribution shown in Fig. 7-8. This effect is the majority of the size dependence in Al(Mg), while the higher-order grain junctions accounted for roughly 22% of grain size-dependence at $X^{tot} = 0.05$ and $T = 700$ K as demonstrated in Fig. 11e and 11f.
- There is a crystallography-dependence of TJ and QN segregation, in analogy to that which is well-known in the GB misorientation space. Characterizing one specific junction can give behavior that deviates significantly from the average. This statistical aspect can be relevant when interpreting sampled experimental results.

Finally, while the results in this study indicate the importance of considering grain junctions in nanocrystalline materials, we are not aware of systematic experimental studies on this issue, almost certainly because of the experimental challenges of producing and characterizing the finest nanocrystalline materials. With improvements in the resolution of STEM [36,56] and APT [35,57–60] we are hopeful that the issue may be addressable in the near future. There are a number of products [61] and simulated systems [25–27,39,62–64] involving alloys with grain sizes at the ~10-40 nm grain scale, so the relevance of these issues for both practical materials and the field of computational materials science could be significant.

8. Acknowledgments

This work was supported by the US Department of Energy award No. DE-SC0020180. N. Tuchinda acknowledges the financial support from Anandamahidol Foundation Scholarship and fruitful discussions with M. Wagih and T. Matson.

9. References

[1] J.W. Cahn, The impurity-drag effect in grain boundary motion, Acta Metallurgica. 10 (1962) 789–798.

[2] K. Lücke, H.P. Stüwe, On the theory of impurity controlled grain boundary motion, Acta Metallurgica. 19 (1971) 1087–1099. https://doi.org/10.1016/0001-6160(71)90041-1.

[3] M. Hillert, Solute drag in grain boundary migration and phase transformations, Acta Materialia. 52 (2004) 5289–5293. https://doi.org/10.1016/j.actamat.2004.07.032.

[4] R.W. Balluffi, S.M. Allen, W.C. Carter, Kinetics of materials, John Wiley & Sons, 2005.
[5] S.G. Kim, Y.B. Park, Grain boundary segregation, solute drag and abnormal grain growth, Acta Materialia. 56 (2008) 3739–3753. https://doi.org/10.1016/j.actamat.2008.04.007.
[6] P. Lejček, Principles of Non-equilibrium Segregation, in: P. Lejcek (Ed.), Grain Boundary Segregation in Metals, Springer Berlin Heidelberg, Berlin, Heidelberg, 2010: pp. 153–171. https://doi.org/10.1007/978-3-642-12505-8_6.
[7] J. Weissmüller, Alloy effects in nanostructures, Nanostructured Materials. 3 (1993) 261–272. https://doi.org/10.1016/0965-9773(93)90088-S.
[8] F. Liu, R. Kirchheim, Nano-scale grain growth inhibited by reducing grain boundary energy through solute segregation, Journal of Crystal Growth. 264 (2004) 385–391. https://doi.org/10.1016/j.jcrysgro.2003.12.021.
[9] J.R. Trelewicz, C.A. Schuh, Grain boundary segregation and thermodynamically stable binary nanocrystalline alloys, Phys. Rev. B. 79 (2009) 094112. https://doi.org/10.1103/PhysRevB.79.094112.
[10] T. Chookajorn, H.A. Murdoch, C.A. Schuh, Design of Stable Nanocrystalline Alloys, Science. 337 (2012) 951–954. https://doi.org/10.1126/science.1224737.
[11] T. Chookajorn, C.A. Schuh, Nanoscale segregation behavior and high-temperature stability of nanocrystalline W–20at.% Ti, Acta Materialia. 73 (2014) 128–138. https://doi.org/10.1016/j.actamat.2014.03.039.
[12] T. Chookajorn, M. Park, C.A. Schuh, Duplex nanocrystalline alloys: Entropic nanostructure stabilization and a case study on W–Cr, J. Mater. Res. 30 (2015) 151–163. https://doi.org/10.1557/jmr.2014.385.
[13] A.R. Kalidindi, T. Chookajorn, C.A. Schuh, Nanocrystalline Materials at Equilibrium: A Thermodynamic Review, JOM. 67 (2015) 2834–2843. https://doi.org/10.1007/s11837-015-1636-9.
[14] P. Lejček, M. Všianská, M. Šob, Recent trends and open questions in grain boundary segregation, J. Mater. Res. 33 (2018) 2647–2660. https://doi.org/10.1557/jmr.2018.230.
[15] T. Chookajorn, C.A. Schuh, Thermodynamics of stable nanocrystalline alloys: A Monte Carlo analysis, Phys. Rev. B. 89 (2014) 064102. https://doi.org/10.1103/PhysRevB.89.064102.
[16] A.R. Kalidindi, C.A. Schuh, Stability criteria for nanocrystalline alloys, Acta Materialia. 132 (2017) 128–137. https://doi.org/10.1016/j.actamat.2017.03.029.
[17] D. McLean, Grain boundaries in metals, Clarendon Press, Oxford, 1957.
[18] E.D. Hondros, M.P. Seah, The theory of grain boundary segregation in terms of surface adsorption analogues, MTA. 8 (1977) 1363–1371. https://doi.org/10.1007/BF02642850.
[19] M. Guttmann, Grain boundary segregation, two dimensional compound formation, and precipitation, MTA. 8 (1977) 1383–1401. https://doi.org/10.1007/BF02642852.
[20] K. Ishida, Effect of grain size on grain boundary segregation, Journal of Alloys and Compounds. 235 (1996) 244–249. https://doi.org/10.1016/0925-8388(95)02094-2.
[21] V.I. Arkharov, N.N. Skornyakov, Changes in the Lattice Parameter of Polycrystalline Solid Solutions and Intercrystalline Internal Adsorption, US Atomic Energy Commission, Technical Information Service, 1953.
[22] J.H. Westbrook, Segregation at grain boundaries, Null. 9 (1964) 415–471. https://doi.org/10.1179/mtlr.1964.9.1.415.
[23] Ming Kaisheng, Li Linlin, Li Zhiming, Bi Xiaofang, Wang Jian, Grain boundary decohesion by nanoclustering Ni and Cr separately in CrMnFeCoNi high-entropy alloys, Science Advances. 5 (n.d.) eaay0639. https://doi.org/10.1126/sciadv.aay0639.

[24] M. Kuzmina, D. Ponge, D. Raabe, Grain boundary segregation engineering and austenite reversion turn embrittlement into toughness: Example of a 9wt.% medium Mn steel, Acta Materialia. 86 (2015) 182–192. https://doi.org/10.1016/j.actamat.2014.12.021.
[25] M. Wagih, C.A. Schuh, Spectrum of grain boundary segregation energies in a polycrystal, Acta Materialia. 181 (2019) 228–237. https://doi.org/10.1016/j.actamat.2019.09.034.
[26] M. Wagih, P.M. Larsen, C.A. Schuh, Learning grain boundary segregation energy spectra in polycrystals, Nat Commun. 11 (2020) 6376. https://doi.org/10.1038/s41467-020-20083-6.
[27] M. Wagih, C.A. Schuh, Grain boundary segregation beyond the dilute limit: Separating the two contributions of site spectrality and solute interactions, Acta Materialia. 199 (2020) 63–72. https://doi.org/10.1016/j.actamat.2020.08.022.
[28] P. Lejček, Effect of Variables on Equilibrium Grain Boundary Segregation, in: P. Lejcek (Ed.), Grain Boundary Segregation in Metals, Springer Berlin Heidelberg, Berlin, Heidelberg, 2010: pp. 103–152. https://doi.org/10.1007/978-3-642-12505-8_5.
[29] F. Tang, X. Liu, H. Wang, C. Hou, H. Lu, Z. Nie, X. Song, Solute segregation and thermal stability of nanocrystalline solid solution systems, Nanoscale. 11 (2019) 1813–1826. https://doi.org/10.1039/C8NR09782H.
[30] L. Huber, R. Hadian, B. Grabowski, J. Neugebauer, A machine learning approach to model solute grain boundary segregation, Npj Comput Mater. 4 (2018) 64. https://doi.org/10.1038/s41524-018-0122-7.
[31] C. White, D. Stein, Sulfur segregation to grain boundaries in Ni 3 Al and Ni 3 (AI, Ti) alloys, Metallurgical Transactions A. 9 (1978) 13–22.
[32] A. Azzalini, A. Capitanio, Statistical applications of the multivariate skew normal distribution, Journal of the Royal Statistical Society: Series B (Statistical Methodology). 61 (1999) 579–602. https://doi.org/10.1111/1467-9868.00194.
[33] G. Palumbo, S.J. Thorpe, K.T. Aust, On the contribution of triple junctions to the structure and properties of nanocrystalline materials, Scripta Metallurgica et Materialia. 24 (1990) 1347–1350. https://doi.org/10.1016/0956-716X(90)90354-J.
[34] N. Wang, G. Palumbo, Z. Wang, U. Erb, K.T. Aust, On the persistence of four-fold triple line nodes in nanostructured materials, Scripta Metallurgica et Materialia. 28 (1993) 253–256. https://doi.org/10.1016/0956-716X(93)90572-A.
[35] B. Färber, E. Cadel, A. Menand, G. Schmitz, R. Kirchheim, Phosphorus segregation in nanocrystalline Ni–3.6 at.% P alloy investigated with the tomographic atom probe (TAP), Acta Materialia. 48 (2000) 789–796. https://doi.org/10.1016/S1359-6454(99)00397-3.
[36] J. Tian, Y.-L. Chiu, Study the grain boundary triple junction segregation of phosphorus in a nickel-base alloy using energy dispersive X-ray spectroscopy on a transmission electron microscope, Materials Characterization. 148 (2019) 156–161. https://doi.org/10.1016/j.matchar.2018.12.021.
[37] K.-M. Yin, A.H. King, T.E. Hsieh, F.-R. Chen, J.J. Kai, L. Chang, Segregation of Bismuth to Triple Junctions in Copper, Microsc Microanal. 3 (1997) 417–422. https://doi.org/10.1017/S1431927697970318.
[38] S.M. Eich, G. Schmitz, Embedded-atom study of grain boundary segregation and grain boundary free energy in nanosized iron–chromium tricrystals, Acta Materialia. 147 (2018) 350–364. https://doi.org/10.1016/j.actamat.2018.01.006.
[39] Y. Purohit, L. Sun, D.L. Irving, R.O. Scattergood, D.W. Brenner, Computational study of the impurity induced reduction of grain boundary energies in nano- and bi-crystalline Al–Pb alloys, Materials Science and Engineering: A. 527 (2010) 1769–1775. https://doi.org/10.1016/j.msea.2009.11.034.

[40] M.I. Mendelev, M. Asta, M.J. Rahman, J.J. Hoyt, Development of interatomic potentials appropriate for simulation of solid–liquid interface properties in Al–Mg alloys, Philosophical Magazine. 89 (2009) 3269–3285.
[41] L. Huber, B. Grabowski, M. Militzer, J. Neugebauer, J. Rottler, Ab initio modelling of solute segregation energies to a general grain boundary, Acta Materialia. 132 (2017) 138–148. https://doi.org/10.1016/j.actamat.2017.04.024.
[42] R.K. Koju, Y. Mishin, Atomistic study of grain-boundary segregation and grain-boundary diffusion in Al-Mg alloys, Acta Materialia. 201 (2020) 596–603. https://doi.org/10.1016/j.actamat.2020.10.029.
[43] L.E. Karkina, I.N. Karkin, A.R. Kuznetsov, I.K. Razumov, P.A. Korzhavyi, Yu.N. Gornostyrev, Solute–grain boundary interaction and segregation formation in Al: First principles calculations and molecular dynamics modeling, Computational Materials Science. 112 (2016) 18–26. https://doi.org/10.1016/j.commatsci.2015.10.007.
[44] P. Hirel, Atomsk: a tool for manipulating and converting atomic data files, Computer Physics Communications. 197 (2015) 212–219.
[45] F. Bachmann, R. Hielscher, H. Schaeben, Texture Analysis with MTEX – Free and Open Source Software Toolbox, SSP. 160 (2010) 63–68. https://doi.org/10.4028/www.scientific.net/SSP.160.63.
[46] S. Plimpton, Fast parallel algorithms for short-range molecular dynamics, Journal of Computational Physics. 117 (1995) 1–19.
[47] W.M. Brown, P. Wang, S.J. Plimpton, A.N. Tharrington, Implementing molecular dynamics on hybrid high performance computers–short range forces, Computer Physics Communications. 182 (2011) 898–911.
[48] W.M. Brown, A. Kohlmeyer, S.J. Plimpton, A.N. Tharrington, Implementing molecular dynamics on hybrid high performance computers–Particle–particle particle-mesh, Computer Physics Communications. 183 (2012) 449–459.
[49] W.M. Brown, M. Yamada, Implementing molecular dynamics on hybrid high performance computers—three-body potentials, Computer Physics Communications. 184 (2013) 2785–2793.
[50] P.M. Larsen, S. Schmidt, J. Schiøtz, Robust structural identification via polyhedral template matching, Modelling and Simulation in Materials Science and Engineering. 24 (2016) 055007.
[51] A. Stukowski, Visualization and analysis of atomistic simulation data with OVITO–the Open Visualization Tool, Modelling and Simulation in Materials Science and Engineering. 18 (2009) 015012.
[52] J.F. Panzarino, T.J. Rupert, Tracking Microstructure of Crystalline Materials: A Post-Processing Algorithm for Atomistic Simulations, JOM. 66 (2014) 417–428. https://doi.org/10.1007/s11837-013-0831-9.
[53] J.D. Honeycutt, H.C. Andersen, Molecular dynamics study of melting and freezing of small Lennard-Jones clusters, Journal of Physical Chemistry. 91 (1987) 4950–4963.
[54] A. Stukowski, Structure identification methods for atomistic simulations of crystalline materials, Modelling Simul. Mater. Sci. Eng. 20 (2012) 045021. https://doi.org/10.1088/0965-0393/20/4/045021.
[55] S. Patala, J.K. Mason, C.A. Schuh, Improved representations of misorientation information for grain boundary science and engineering, Progress in Materials Science. 57 (2012) 1383–1425. https://doi.org/10.1016/j.pmatsci.2012.04.002.
[56] H. Wen, B. Zhao, J. Zhou, X. Dong, Q. Chen, F. Sun, L. Zhang, Early segregation and precipitation at triple junction in an alumina-forming austenitic steel, Materials Letters. 283 (2021) 128802. https://doi.org/10.1016/j.matlet.2020.128802.

[57] S. Ruan, K.L. Torres, G.B. Thompson, C.A. Schuh, Gallium-enhanced phase contrast in atom probe tomography of nanocrystalline and amorphous Al–Mn alloys, Ultramicroscopy. 111 (2011) 1062–1072. https://doi.org/10.1016/j.ultramic.2011.01.026.
[58] A.J. Detor, M.K. Miller, C.A. Schuh, Measuring grain-boundary segregation in nanocrystalline alloys: direct validation of statistical techniques using atom probe tomography, Philosophical Magazine Letters. 87 (2007) 581–587. https://doi.org/10.1080/09500830701400125.
[59] P. Stender, Z. Balogh, G. Schmitz, Triple junction segregation in nanocrystalline multilayers, Phys. Rev. B. 83 (2011) 121407. https://doi.org/10.1103/PhysRevB.83.121407.
[60] Z. Balogh, P. Stender, M.R. Chellali, G. Schmitz, Investigation of Interfaces by Atom Probe Tomography, Metall and Mat Trans A. 44 (2013) 4487–4495. https://doi.org/10.1007/s11661-012-1517-6.
[61] C.A. Schuh, K. Lu, Stability of nanocrystalline metals: The role of grain-boundary chemistry and structure, MRS Bulletin. 46 (2021) 225–235. https://doi.org/10.1557/s43577-021-00055-x.
[62] A. Detor, C. Schuh, Grain boundary segregation, chemical ordering and stability of nanocrystalline alloys: Atomistic computer simulations in the Ni–W system, Acta Materialia. 55 (2007) 4221–4232. https://doi.org/10.1016/j.actamat.2007.03.024.
[63] J.D. Rittner, D. Udler, D.N. Seidman, Y. Oh, Atomic Scale Structural Effects on Solute-Atom Segregation at Grain Boundaries, Phys. Rev. Lett. 74 (1995) 1115–1118. https://doi.org/10.1103/PhysRevLett.74.1115.
[64] C.J. O'Brien, C.M. Barr, P.M. Price, K. Hattar, S.M. Foiles, Grain boundary phase transformations in PtAu and relevance to thermal stabilization of bulk nanocrystalline metals, Journal of Materials Science. 53 (2018) 2911–2927. https://doi.org/10.1007/s10853-017-1706-1.

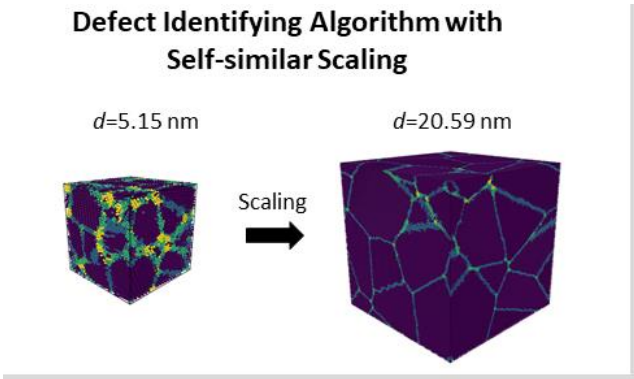

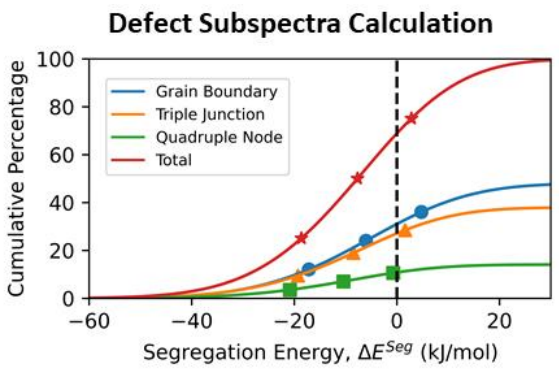

Thermodynamic Framework & Grain-size Dependency Caused by:

(i) Spectrality

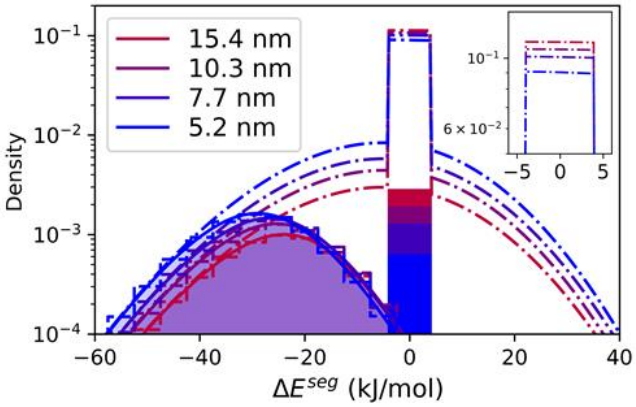

(ii) Triple Junctions and Quadruple Nodes